SCIENTIFIC REP😃RTS

OPEN

Confined SnO$_2$ quantum-dot clusters in graphene sheets as high-performance anodes for lithium-ion batteries

Chengling Zhu[1], Shenmin Zhu[1], Kai Zhang[1], Zeyu Hui[1], Hui Pan[1], Zhixin Chen[2], Yao Li[1], Di Zhang[1] & Da-Wei Wang[3]

Construction of metal oxide nanoparticles as anodes is of special interest for next-generation lithium-ion batteries. The main challenge lies in their rapid capacity fading caused by the structural degradation and instability of solid-electrolyte interphase (SEI) layer during charge/discharge process. Herein, we address these problems by constructing a novel-structured SnO$_2$-based anode. The novel structure consists of mesoporous clusters of SnO$_2$ quantum dots (SnO$_2$ QDs), which are wrapped with reduced graphene oxide (RGO) sheets. The mesopores inside the clusters provide enough room for the expansion and contraction of SnO$_2$ QDs during charge/discharge process while the integral structure of the clusters can be maintained. The wrapping RGO sheets act as electrolyte barrier and conductive reinforcement. When used as an anode, the resultant composite (MQDC-SnO$_2$/RGO) shows an extremely high reversible capacity of 924 mAh g^{-1} after 200 cycles at 100 mA g^{-1}, superior capacity retention (96%), and outstanding rate performance (505 mAh g^{-1} after 1000 cycles at 1000 mA g^{-1}). Importantly, the materials can be easily scaled up under mild conditions. Our findings pave a new way for the development of metal oxide towards enhanced lithium storage performance.

Anode materials with high capacities and excellent cycling stability have been searched for more than ten years[1–9] to replace the conventionally used graphite which possess a low theoretical capacity of 372 mAh g^{-1} in lithium-ion batteries (LIBs). With high theoretical capacities (~1000 mAh g^{-1}), many metal oxides are deemed as the promising materials for next-generation LIB anode[4–9]. Unfortunately, two obstacles exist to hinder their practical applications: one is the intrinsic low electrical conductivity and low Li$^+$ diffusion rate in bulk materials, resulting in great mismatch between the actual capacity and the theoretical capacity, especially at high current densities[5,10]; the other is the ceaseless generation and rupture of solid–electrolyte interphase (SEI) layer, caused by the pulverization and agglomeration of anode materials due to their significant volume change during lithiation/delithiation process. The proliferous SEI layer gives rise to the continuous consumption of electrolyte and active material, and takes the blame for capacity fading[11,12].

Diminishing the size of anode materials to nanoscale, and further to quantum-dot (QD) scale is proven to be an effective route to shorten the diffusion length of Li$^+$[13]. Nevertheless, the specific surface area of particles would rise with the decrease in particle size, causing more exposed surfaces for SEI formation[14,15]. Assembling nanoparticles into clusters might be an efficient approach to deal with this problem. In 2014, Cui *et al.* designed and fabricated a porous nanoparticle–cluster structure in Si-based LIB anode[16]. SiO$_2$ sacrificial layer was employed to create enough void space around individual Si nanoparticles, which were then encapsulated by amorphous carbon through an emulsion process and the subsequent pyrolysis of resorcinol–formaldehyde resin. The carbon shell provides both an effective barrier against excessive formation of SEI and high electrical conductivity. Unfortunately, the emulsion operation used is complex. The exclusive employment of SiO$_2$ sacrificial layer to create void space around individual Si particles and the subsequent unhandy HF etching process, limit the application of this elaborate Si-based anode, and make it a great challenge to apply the synthesis route in other

[1]State Key Laboratory of Metal Matrix Composites, Shanghai Jiao Tong University, Shanghai 200240, P. R. China. [2]School of Mechanical, Materials & Mechatronics Engineering, University of Wollongong, Wollongong, NSW 2522, Australia. [3]School of Chemical Engineering, UNSW Australia, UNSW Sydney, NSW 2052, Australia. Correspondence and requests for materials should be addressed to S.Z. (email: smzhu@sjtu.edu.cn)
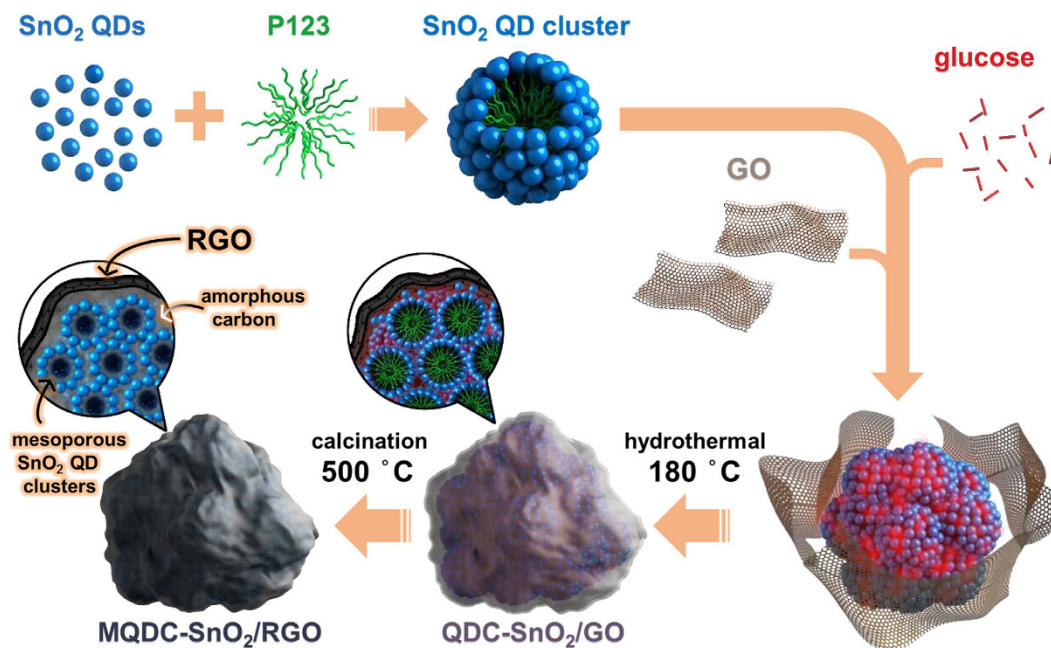
Figure 1. Schematic of the synthesis route of MQDC-SnO$_2$/RGO.

anode materials, such as SnO$_2$. Moreover, the insufficient conductivity of the amorphous carbon coating could be improved further.

Herein, we develop an easy and cheap route of fabricating a novel and hierarchical structure of SnO$_2$-based anode, in which SnO$_2$ QD clusters with internal mesopores are wrapped dexterously with reduced graphene oxide sheets (denoted as MQDC-SnO$_2$/RGO). The superiority of this novel structure lies in the multiple virtues: (1) the ultra-small size (~3 nm) of the SnO$_2$ QDs and the mesopores assembled in clusters of micrometer size would shorten the diffusion length of Li$^+$ and provide extensive surface for lithiation/delithiation reaction; (2) the amorphous carbon matrix around the SnO$_2$ QDs and the RGO shell outside the clusters greatly reinforce the electronic conductivity of the composite; (3) the SnO$_2$ QDs are intactly encapsuled in the dual carbon coating layers (amorphous carbon and RGO), which restrain the formation of SEI. When used as anode material, the resultant MQDC-SnO$_2$/RGO shows superior performances.

Results

The synthesis route of MQDC-SnO$_2$/RGO is illustrated in Fig. 1. Firstly, SnO$_2$ QDs were prepared in aqueous environment at room temperature (see Supplementary Fig. S1 online), resulting in nanoparticles of ~3 nm as observed by TEM and HRTEM (Supplementary Fig. S2), close to the computed value from the X-ray diffraction (XRD) (Supplementary Fig. S3, Table S1). The strong quantum confinement effect detected by ultraviolet-visible (UV-vis) absorption spectroscopy indicates that the nanoparticles are quantum-dots (Supplementary Fig. S4). Then P123 was added, causing the spontaneous formation of SnO$_2$ QD clusters in hydrosol, as detected by dynamic light scattering (DLS) (Supplementary Fig. S5). Subsequent introduction of graphene oxide (GO) and glucose were performed, and hydrothermal process was then conducted to partly reduce GO with glucose as reductant[17,18], so as to induce π–π stacking between RGO sheets and reach a wrapping effect on the surface of SnO$_2$ QD clusters. The composite was denoted as QDC-SnO$_2$/GO after hydrothermal process. QDC-SnO$_2$/GO was calcined under N$_2$ to pyrolyze P123 and convert glucose to carbon. The pyrolysis of P123 creates mesopores between SnO$_2$ particles and the carbon transformed from glucose encapsulates the SnO$_2$ QDs. Thus the resultant MQDC-SnO$_2$/RGO composite was obtained.

The composition of MQDC-SnO$_2$/RGO was determined with XRD (Fig. 2). The peaks on the XRD pattern of the composite before calcination, QDC-SnO$_2$/GO, can be assigned to SnO$_2$, SnO and a small quantity of Sn. The elemental Sn is attributed to the reducing effect of glucose during hydrothermal process. At the same time GO is reduced to RGO partly also, seen from the absence of the characteristic peak of GO at 10.5°. After calcined at 500 °C, it can been found from the XRD pattern of MQDC-SnO$_2$/RGO that Sn and most SnO convert to SnO$_2$, leaving only negligible quantity of SnO.

Secondary electron images under scanning electron microscope (SEM) (Fig. 3a,b) reveal the surface morphology of MQDC-SnO$_2$/RGO. Clusters of 3–5 μm have been wrapped tightly by RGO sheets, with a plicated appearance. It appears that the distribution of SnO$_2$ in RGO sheets is fairly even in the energy-dispersive X-ray elemental mapping result (Fig. 3c). No scattered SnO$_2$ particle outside the clusters was found in the secondary electron images. The fine nano-structure of MQDC-SnO$_2$/RGO is further investigated by TEM (Fig. 3d,e and Supplementary Fig. S7). The SnO$_2$ QD clusters wrapped by thin RGO sheets (with lots of wrinkled area) can be clearly observed (Fig. 3d). Within the clusters there are plentiful pores with pore size under 10 nm as shown in Fig. 3e.
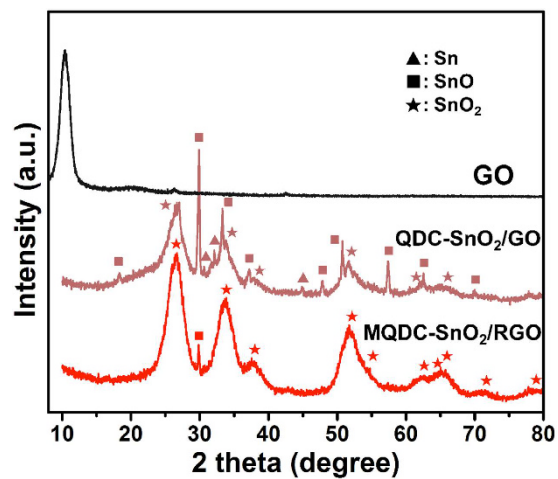
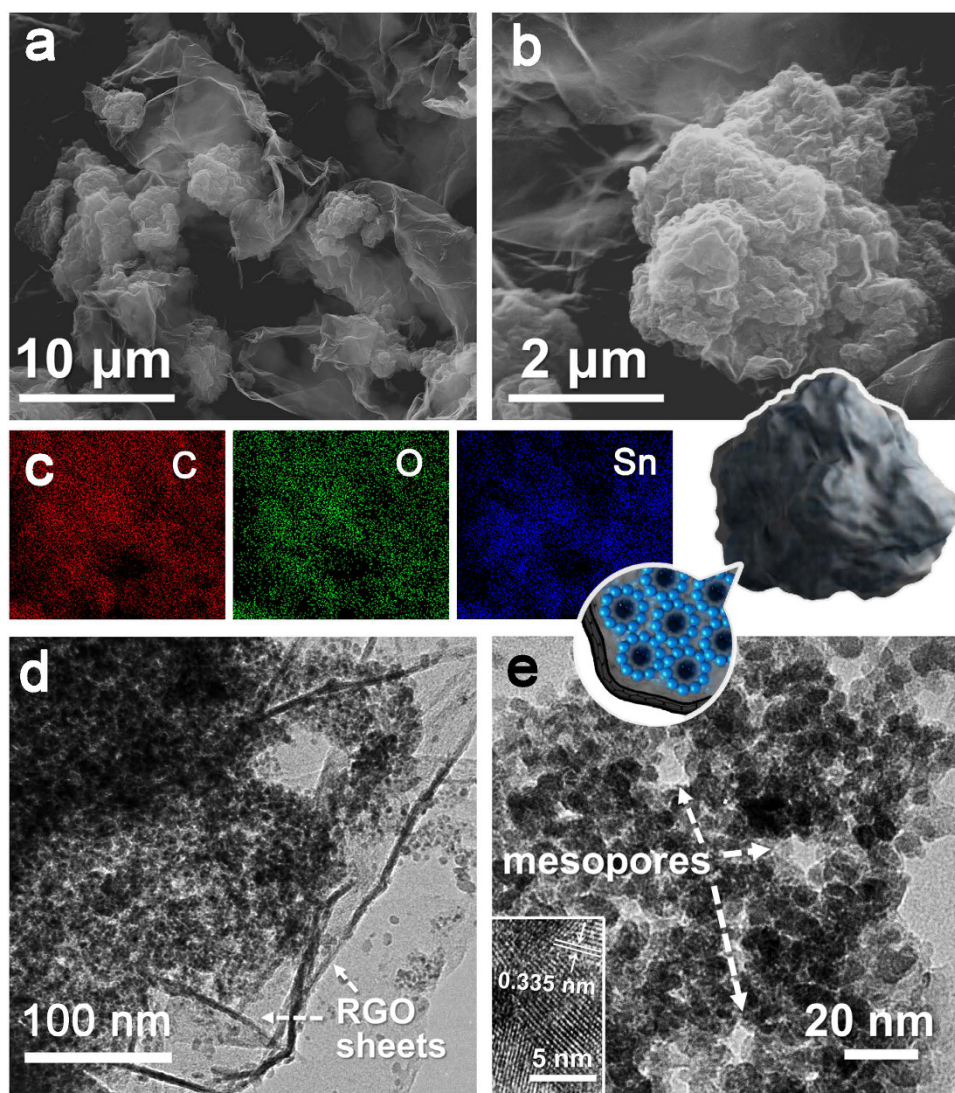**Figure 2.** XRD pattern of GO, MQDC-SnO$_2$/RGO and QDC-SnO$_2$/GO.

Figure 3. (**a,b**) Secondary electron images of MQDC-SnO$_2$/RGO in different magnifications. (**c**) Elemental mapping of MQDC-SnO$_2$/RGO corresponding to the area in (**a**). (**d,e**) TEM images of MQDC-SnO$_2$/RGO.

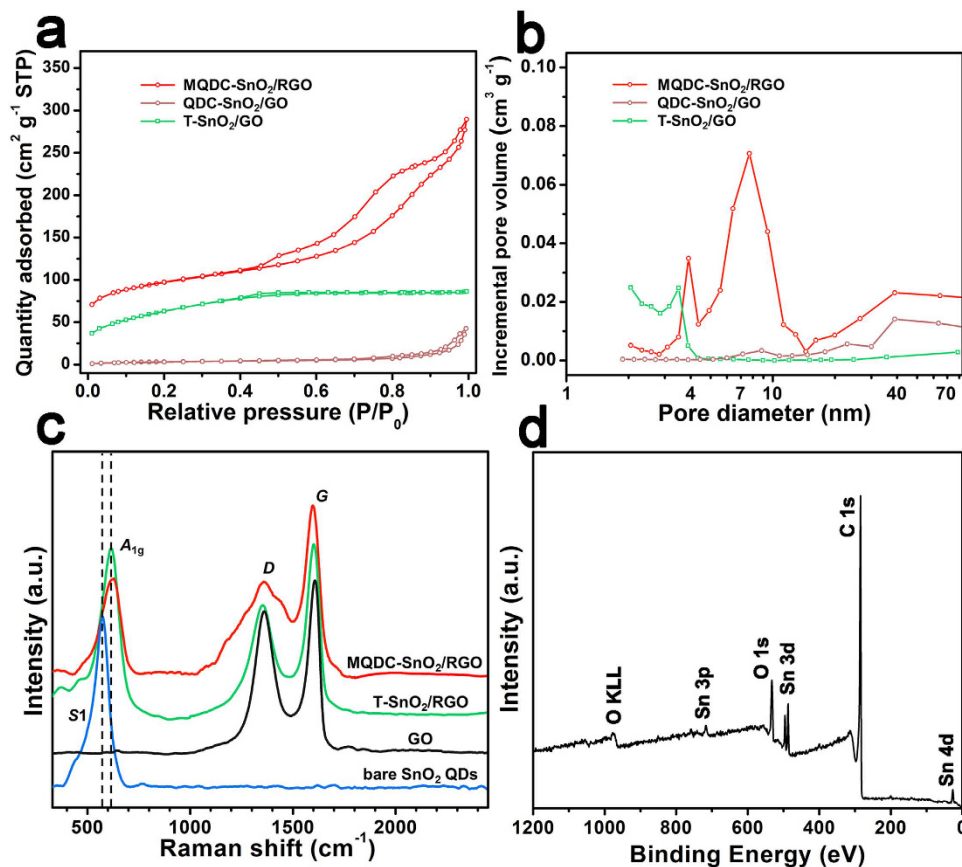**Figure 4.** (**a**) Nitrogen adsorption/desorption isotherms and (**b**) pore size distribution of MQDC-SnO₂/RGO, QDC-SnO₂/GO and T- SnO₂/RGO. (**c**) Raman spectra of MQDC-SnO₂/RGO, T-SnO₂/RGO, GO and bare SnO₂ QDs. (**d**) Survey XPS spectra of MQDC-SnO₂/RGO.

It should be mentioned that glucose plays an indispensable role in the formation of this wrapped cluster structure. As a comparison, a sample prepared under the same condition as MQDC-SnO₂/RGO but without the addition of glucose is denoted as T-SnO₂/RGO. Contrast to MQDC-SnO₂/RGO, T-SnO₂/RGO demonstrates a flat and dense surface, with SnO₂ QDs tiled on RGO sheets, while no cluster structure can be found from its SEM images (Supplementary Fig. S6). As glucose molecules are of abundant hydroxyl groups, they tend to form hydrogen bonds with the oxygen atoms on the surface of SnO₂ QDs and the epoxy groups on GO sheets[17]. During the hydrothermal process, these bonds can crosslink GO sheets and SnO₂ QDs and stabilize the cluster structure of SnO₂ QDs. After calcination, glucose decomposes into amorphous carbon that covers on the surface of SnO₂ QDs, and thus the cluster structure forms in MQDC-SnO₂/RGO, as shown in Fig. 3a.

The Brunauer–Emmett–Teller (BET) analysis results of nitrogen adsorption measurements show that MQDC-SnO₂/RGO has a high specific surface area (SSA) of 337 m² g⁻¹ (Fig. 4a). Moreover, the bi-distribution of the mesopores is found in Fig. 4b, one at 4 nm and another at 8 nm. The pores with size of 8 nm should be attributed to the addition of P123[19]. The formation of the smaller-size pores (4 nm) is deemed to be related to the native space among SnO₂ QDs. It is deduced that P123 decomposes at 500 °C, leaving large amounts of mesopores in MQDC-SnO₂/RGO. As a comparison, T-SnO₂/RGO has an SSA of 230 m² g⁻¹, while mesopores around 8 nm cannot be found. Because P123 was also added during the synthesis process, the lack of pores around 8 nm in T-SnO₂/RGO undoubtedly results from the absence of glucose. Without the reinforcement of the amorphous carbon derived from glucose, the pores left by P123 in T-SnO2/RGO collapse completely during the calcination process.

The carbon materials in MQDC-SnO₂/RGO have been characterized using Raman spectroscopy (Fig. 4c). The intensity ratio of D band (~1350 cm⁻¹) and G band (~1582 cm⁻¹) (denoted as I_D/I_G) has long been introduced as an index of disorder in carbon materials and also a reference to check the extent of the reduction of GO[20–22]. I_D/I_G for MQDC-SnO₂/RGO and T-SnO₂/RGO were calculated to be 0.58 and 0.65, respectively. They are much smaller than that of the GO counterpart (0.82) and thus indicate that the GO was reduced to RGO in the synthesis. The broadening of D band of MQDC-SnO₂/RGO should be attributed to the glucose-derived amorphous carbon[23], which is not observed in that of T-SnO₂/RGO. The $S1$ band (~570 cm⁻¹) of bare SnO₂ QDs shifts to a new position that centers at mode A_{1g} (~630 cm⁻¹) in the spectra of MQDC-SnO₂/RGO and T-SnO₂/RGO. This shift is caused by slightly grain growth and the higher crystallinity of SnO₂ QDs after calcination[24].

The content of SnO₂ in MQDC-SnO₂/RGO was measured to be 48 wt% by thermogravimetric analysis (TGA) (Supplementary Fig. S8). However, it was found in the X-ray photoelectron spectroscopy (XPS) survey
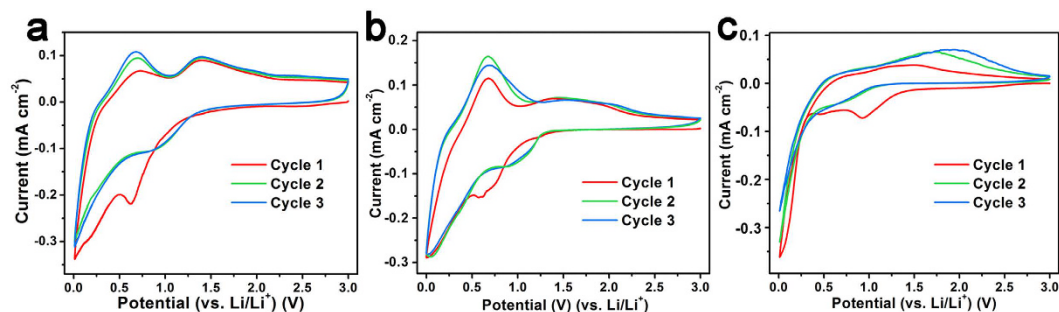
Figure 5. The CVs of (**a**) MQDC-SnO$_2$/RGO, (**b**) T-SnO$_2$/RGO, and (**c**) bare SnO$_2$ QDs, recorded at scan rate of 0.05 mV s^{-1}.

spectrum of MQDC-SnO$_2$/RGO that the peak intensity of C 1s is much stronger than Sn 3d, 4d and 3p peaks (Fig. 4d), and the mass concentrations of C and Sn elements were computed to be 82.40% and 8.06%, respectively (Supplementary Table S2). This result shows a great disparity with the TGA result. This is unsurprising as the photoelectron signal detected by XPS is generally restricted at the surface of samples. Since the SnO$_2$ QDs in MQDC-SnO$_2$/RGO are wrapped by amorphous carbon and RGO, the signals from Sn could not be clearly detected by XPS. Therefore, the undervalued content of Sn from the XPS result is deemed as an indirect, yet forceful proof of the unique SnO$_2$-wrapped-in-RGO structure.

Clearly, the synthesized MQDC-SnO$_2$/RGO has the structure of mesoporous SnO$_2$ QD clusters wrapped internally with amorphous carbon and externally with RGO sheets. Although MQDC-SnO$_2$/RGO has such a sophisticated structure, its synthesis route is practically simple and without involving any complex process like emulsion operation or using a template.

The electrochemical performances have been tested by assembling the materials into coin-type half cells. Figure 5 represents the corresponding cyclic voltammograms (CVs). The reduction peaks between 0.5 V to 1.0 V in the first cycle of MQDC-SnO$_2$/RGO, T-SnO$_2$/RGO and bare SnO$_2$ QDs are the sign of the SEI phase formation, ascribed to the reduction of SnO$_2$ to Sn by Li$^+$, which is usually regarded to be irreversible. However, the stable oxidation peak at 1.40 V and retained reduction peak at 0.95 V in the succeeding cycles of MQDC-SnO$_2$/RGO indicate a partial reversibility of the conversion between SnO$_2$ and Sn. The partial reversibility can contribute additional capacity to the theoretical base (782 mAh g^{-1})[25,26], but it is not observed in the CV of bare SnO$_2$ QDs and is inconspicuous in that of T-SnO$_2$/RGO. The theoretically reversible alloying/dealloying reaction of Li$_x$Sn is recognized as the reduction peak at 0.01 V and oxidation peak at 0.68 V. This reduction peak gradually weakens for bare SnO$_2$ QDs but maintains steady for MQDC-SnO$_2$/RGO and T-SnO$_2$/RGO. Moreover, the oxidation peak at 0.68 V for MQDC-SnO$_2$/RGO shows a gradual upshift compared to that of the bare SnO$_2$ QDs. This upshift indicates very different electrochemical properties of MQDC-SnO$_2$/RGO from that of bare SnO$_2$ QDs.

Galvanostatic charge/discharge cycling results are shown in Fig. 6a. For bare SnO$_2$ QDs, the initial discharge and charge capacities reached 1522 and 785 mAh g^{-1} respectively, but declined rapidly afterwards and retained only 33 mAh g^{-1} after 200 cycles. Although the ultra-small size of SnO$_2$ QDs would drastically shorten the diffusion length of Li$^+$ and lead to high specific capacities during the starting several cycles, its quantum confinement effect may cause an augment of charge transfer resistance at the same time[27]. More seriously, the ultra-small size provides large surface area for the formation of SEI, and the bare morphology cannot stand severe pulverization and agglomeration. Similar results were obtained for T-SnO$_2$/RGO. The MQDC-SnO$_2$/RGO composite with the novel nano-structure is designed to break these limitations. The discharge and charge capacities reach 1620 and 960 mAh g^{-1} in the first cycle, fade to 640 mA g h^{-1} after 10 cycles, and then exhibit a fluctuant recover extending along the subsequent cycles, seen more clearly in the voltage-specific capacity profile (Supplementary Fig. S10). This may be resulted from the novel nano-structure of MQDC-SnO$_2$/RGO compared to bare SnO$_2$ QDs and T-SnO$_2$/RGO. As the SnO$_2$ QD clusters are tightly wrapped by RGO sheets and hold a porous internal structure, the compact RGO wrap stabilizes SEI layers and confines them outside the wrapped clusters, and the ample pore space can sustain the significant volume change of SnO$_2$ QDs, and thus lead to a stable structure of the SnO$_2$ QD clusters. The RGO-wrapped structure of MQDC-SnO$_2$/RGO is well retained during its service, attested by the SEM observation after 100 cycles (Supplementary Fig. S11). The charge capacity of MQDC-SnO$_2$/RGO reached 924 mAh g^{-1} after 200 cycles (that is 96% of the first cycle capacity, and 144% of the 10th cycle), much higher than the theoretical specific capacity of either SnO$_2$ (782 mAh g^{-1}) or graphene (744 mAh g^{-1}). It is probably due to the partial reversible conversion between SnO$_2$ and Sn that verified by the CV results (Fig. 5). Similar fade-recover results were also obtained at a higher charge/discharge current of 1000 mA g^{-1}, where a high specific capacity of 505 mAh g^{-1} and a high coulombic efficiency up to 99.8% are retained after 1000 cycles (Fig. 6b). Furthermore, the capacities, the cyclic stability and the rate performance of MQDC-SnO$_2$/RGO are dominant to many SnO$_2$/graphene anode materials with similar structure to T-SnO$_2$/RGO reported in literatures (Supplementary Table S3), and the superiority of MQDC-SnO$_2$/RGO as LIB anode is convincingly demonstrated.

The rate performance of MQDC-SnO$_2$/RGO is much superior to bare SnO$_2$ QDs and T-SnO$_2$/RGO, as shown in Fig. 6c. The discharge capacities of the bare SnO$_2$ QDs are comparable to those of MQDC-SnO$_2$/RGO in the first few cycles, and in the first 16 cycles at 100, 200, and 500 mA g^{-1}, the discharge capacities of T-SnO$_2$/RGO are even higher than MQDC-SnO$_2$/RGO. However, the discharge capacities of bare SnO$_2$ QDs and T-SnO$_2$/RGO fade rapidly to only 6 and 65 mAh g^{-1} respectively at 3000 mA g^{-1} after 28 cycles while MQDC-SnO$_2$/RGO reaches
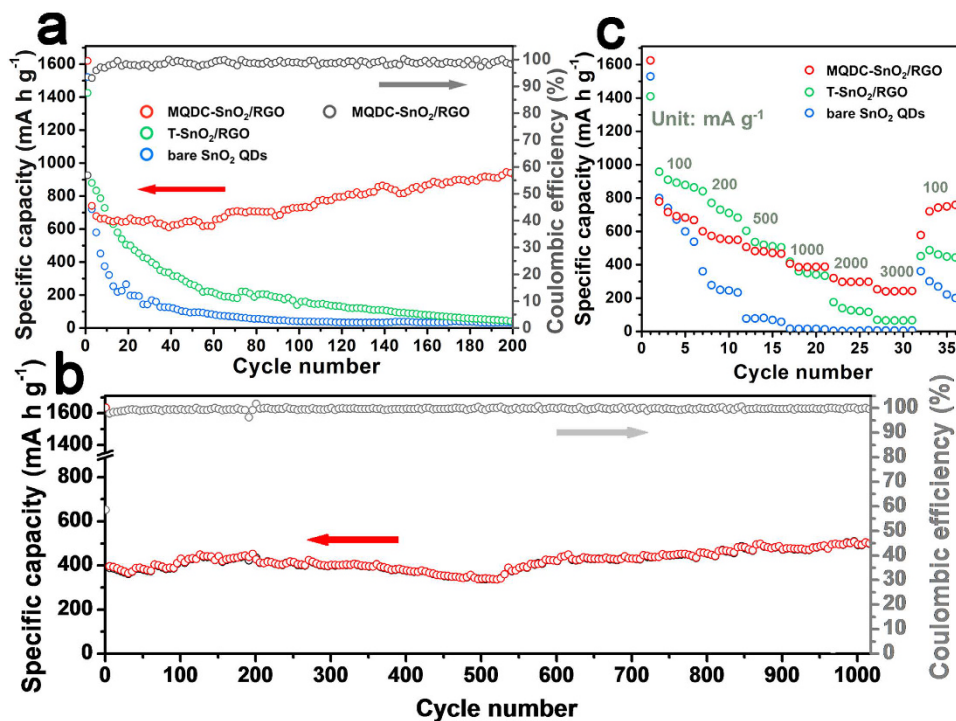
Figure 6. (**a**) Specific discharge capacity and coulombic efficiency of MQDC-SnO$_2$/RGO at 100 mA g^{-1}, in comparison to the performances of T-SnO$_2$/RGO and bare SnO$_2$ QDs at the same current density. (**b**) Cyclic performance of MQDC-SnO$_2$/RGO at 1000 mA g^{-1} (5 charge/discharge cycles at 100 mA g^{-1} were conducted initially as an activation process). (**c**) Rate performance of MQDC-SnO$_2$/RGO, T-SnO$_2$/RGO and SnO$_2$ QDs (discharge capacities). The varying current is 100 mA g^{-1} for 6 cycles, 200, 500, 1000, 2000 and 3000 mA g^{-1} for 5 cycles each, and finally 100 mA g^{-1} for 5 cycles.

240 mAh g^{-1} at the same current. Though the capacity of SnO$_2$ QDs recovers to 362 mAh g^{-1} when the current is brought down back to 100 mA g^{-1}, it fades badly to 201 mAh g^{-1} in 5 cycles, and a similar fading process was also obtained for T-SnO$_2$/RGO. However, the ingenious structure of MQDC-SnO$_2$/RGO induces a stable capacity recovery (759 mAh g^{-1}) when the current is brought down, which is distinct from the bare SnO$_2$ QDs or T-SnO$_2$/RGO. It is inferred that during the cycles at large currents, the mesopores in SnO$_2$ QD clusters provide fast access to Li$^+$ while the well conductive RGO sheets give fast access to electrons. The synergistic effect promotes sufficient lithiation/delithiation reaction and maintains the structural integrity of the composite. This echoes the rate performance of the graphene-based mesoporous SnO$_2$ composite previously reported[28]. However, the capacity recover phenomenon exhibited by MQDC-SnO$_2$/RGO and profitted from its unique structure has not been reported by other researchers.

Electrochemical impedance spectra (EIS) of MQDC-SnO$_2$/RGO, T-SnO$_2$/RGO and bare SnO$_2$ QDs give corroborative evidences of the electrical conductivity provided by RGO sheets, and the suppressed stable formation of SEI in MQDC-SnO$_2$/RGO after charge/discharge cycles. As shown in the Nyquist plots (Fig. 7), the semicircle in the high-medium-frequency region of bare SnO$_2$ QDs obviously separates into two semicircles, one in the high-frequency region and another in the medium-frequency region. The medium-frequency semicircle is related to the charge-transfer resistance inside an electrode[29], which can be obviously observed in the Nyquist plot of bare SnO$_2$ but not observed in that of MQDC-SnO$_2$/RGO or T-SnO$_2$/RGO. This trait indicates a dominant electrical conductivity of the RGO-composed samples to bare SnO$_2$ QDs. MQDC-SnO$_2$/RGO and T-SnO$_2$/RGO each has one semicircle in the high-frequency region and the former has the smallest one. The high-frequency region is related to the diffusion of Li$^+$ in SEI layer, and the smaller this semicircle is, the less SEI is in the system[9]. Hence, the formation of the SEI layer was significantly suppressed in MQDC-SnO$_2$/RGO because it has the smallest semicircle in the high frequency region among all the three samples. The combination of less SEI layer and higher electrical conductivity resulted in the excellent electrochemical performances of MQDC-SnO$_2$/RGO.

Discussion

In conclusion, an ingenious RGO-wrapped mesoporous SnO$_2$ QD cluster composite (MQDC-SnO$_2$/RGO) for LIB anode has been designed and successfully fabricated. In this novel architecture, the ultra-small size of SnO$_2$ QDs down to ~3 nm surrounded with the mesopores in the SnO$_2$ QD clusters can provide short diffusion length of Li$^+$ and the RGO sheets give fast access to electrons and depress the formation of SEI, leading to a stable structure. These two factors let MQDC-SnO$_2$/RGO have a much high reversible capacity of 924 mAh g^{-1} after 200 cycles at 100 mA g^{-1}, and excellent rate performance, reaching 240 mAh g^{-1} at 3000 mA g^{-1}. Importantly, the synthesis of the material can be easily scaled up at room temperature, which is a milestone for its practical use. This

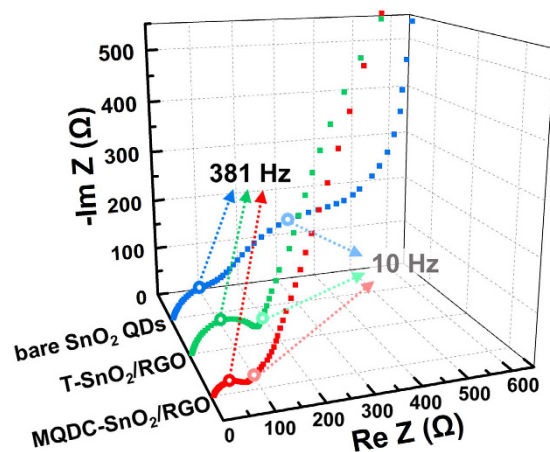**Figure 7.** Nyquist plots of MQDC-SnO$_2$/RGO, T-SnO$_2$/RGO and bare SnO$_2$ QDs, measured by EIS with an amplitude of 5.0 mV and the frequency ranging from 100 kHz to 0.01 Hz, after 3 cycles of galvanostatic charge/discharge at 100 mA g^{-1}.

work opens a new route for the design and construction of other metal oxide clusters with enhanced battery performance, such as Fe$_3$O$_4$, Fe$_2$O$_3$ and MnO$_2$. It should be mentioning that the rate performance of MQDC-SnO$_2$/RGO has much room to be improved, which is deemed to be reached by constructing mesopores not only inside the clusters, but also on the RGO shell.

Methods

Synthesis of SnO$_2$ quantum dots (SnO$_2$ QDs).   The SnO$_2$ QDs were synthesized as hydrosol by peptizing the precipitate product of reacting tin tetrachloride (SnCl$_4$) aqueous solution with ammonium hydroxide (NH$_4$OH). In a typical synthesis, SnCl$_4$·5H$_2$O (17.53 g) was dissolved in deionized water (100 mL), followed by adding ammonium hydroxide (25 wt%, 10 mL) under rapid stirring. The precipitate was separated out, and washed with deionized water several times until its pH = 9.0. Deionized water (20 mL) was added into the washed precipitate, and the white suspension obtained was stirred continuously to accelerate peptization. When the suspension turned semitransparent, the unpeptized part was removed by high-speed centrifugation, and thus the transparent clear SnO$_2$ QD hydrosol was obtained.

Synthesis of MQDC-SnO$_2$/RGO composite.   GO was prepared by the well-known Hummers method[30] and dispersed in deionized water (5 g L^{-1}). P123 (0.2 g) was dissolved into the SnO$_2$ QD hydrosol (100 g L^{-1}, 3 mL), and after 10 min of stirring, glucose (0.18 g) and the as-prepared GO suspension (2 mL) was added. The mixture was transferred into a polytetrafluoroethylene autoclave and kept 180 °C for 3 h. Then, the precipitate was lyophilized and calcined in nitrogen at 500 °C to get MQDC-SnO$_2$/RGO composite. For the synthesis of tiled SnO$_2$ on reduced graphene oxide (T-SnO$_2$/RGO), same operations were conducted except the absence of glucose.

Materials Characterization.   XRD patterns were recorded on a Rigaku D/max2550VL/PC system, using Cu $K\alpha$ radiation. DLS measurements were operated on Malvern Zetasizer Nano ZS. SEM (JEOL JSM-6360LV, 15 kV), TEM and HRTEM (JEOL 2010, 200 kV) were used to observe the morphology of the samples. Nitrogen adsorption measurements were performed at 77 K on a Micromeritics ASAP 2020. UV-vis absorption spectra were measured on a Perkin-Elmer 330 spectrophotometer. Raman spectra were collected on a Renishaw in Via Raman microscope. TGA was conducted on a Perkin-Elmer TGA-7 Thermal Analyzer under O$_2$ flow, with a heating rate of 20 °C min^{-1}. XPS spectra were recorded on a Perkin-Elmer PHI-5400 spectrometer, using Mg $K\alpha$ radiation as the excitation source.

Electrochemical Measurements.   The samples were assembled into 2016 coin-type half cells with Li^0 foil as counter electrodes. To prepare working electrode, the samples were mixed with acetylene black and PVDF by a mass ratio of 8:1:1, and coated on a copper foil. Polypropylene membrane (Celgard 2500) was employed as separator. LiPF$_6$ (1 M) in ethylene carbonate (EC) and diethyl carbonate (DEC) (1:1, v/v) was used as electrolyte. Cyclic voltammetry and electrochemical impedance spectroscopy tests were done on a CHI-660D electrochemical workstation. Galvanostatic cycling tests were conducted on a LAND-CT2001A battery test system, with a voltage window of 0.01–3.00 V vs. Li/Li$^+$.

References

1. Yoshio, M. *et al.* Carbon-coated Si as a lithium-ion battery anode material. *J. Electrochem. Soc.* **149**, A1598–A1603 (2002).
2. Shi, Y. *et al.* Self-assembly of hierarchical MoS$_x$/CNT nanocomposites (2 < x < 3): towards high performance anode materials for lithium ion batteries. *Sci. Rep.* **3**, 2169 (2013).
3. Gao, X. *et al.* Novel germanium/polypyrrole composite for high power lithium-ion batteries. *Sci. Rep.* **4**, 6095 (2014).
4. Reddy, A. L. M., Shaijumon, M. M., Gowda, S. R. & Ajayan, P. M. Coaxial MnO$_2$/carbon nanotube array electrodes for high-performance lithium batteries. *Nano Lett.* **9**, 1002–1006 (2009).
5. Li, Y. *et al.* Carbon-coated SnO$_2$@C with hierarchically porous structures and graphite layers inside for a high-performance lithium-ion battery. *J. Mater. Chem.* **22**, 2766–2773 (2012).

6. Su, D., Ford, M. & Wang, G. Mesoporous NiO crystals with dominantly exposed {110} reactive facets for ultrafast lithium storage. *Sci. Rep.* **2,** 924 (2012).
7. Yang, S. *et al.* Porous iron oxide ribbons grown on graphene for high-performance lithium storage. *Sci. Rep.* **2,** 427 (2012).
8. Ding, L. *et al.* Ultrasmall SnO$_2$ Nanocrystals: Hot-bubbling synthesis, encapsulation in carbon layers and applications in high capacity Li-ion storage. *Sci. Rep.* **4,** 4647 (2014).
9. Kang, D., Liu, Q., Chen, M., Gu, J. & Zhang, D. Spontaneous cross-linking for fabrication of nanohybrids embedded with size-controllable particles. *ACS Nano* **10,** 889–898 (2015).
10. Kang, E. *et al.* Fe$_3$O$_4$ nanoparticles confined in mesocellular carbon foam for high performance anode materials for lithium-ion batteries. *Adv. Funct. Mater.* **21,** 2430–2438 (2011).
11. Huang, J. Y. *et al. In situ* observation of the electrochemical lithiation of a single SnO$_2$ nanowire electrode. *Science* **330,** 1515–1520 (2010).
12. Wang, R., Xu, C., Sun, J. & Gao, L. Three-dimensional Fe$_2$O$_3$ nanocubes/nitrogen-doped graphene aerogels: Nucleation mechanism and lithium storage properties. *Sci. Rep.* **4,** 7171 (2014).
13. Kim, C., Noh, M., Choi, M., Cho, J. & Park, B. Critical size of a nano SnO$_2$ electrode for Li-secondary battery. *Chem. Mater.* **17,** 3297–3301 (2005).
14. Lee, S. H. *et al.* Self-assembled Fe$_3$O$_4$ nanoparticle clusters as high-performance anodes for lithium ion batteries via geometric confinement. *Nano Lett.* **13,** 4249–4256 (2013).
15. Zhang, X., Jiang, B., Guo, J., Xie, Y. & Tang, L. Large and stable reversible lithium-ion storages from mesoporous SnO$_2$ nanosheets with ultralong lifespan over 1000 cycles. *J. Power Sources* **268,** 365–371 (2014).
16. Liu, N. *et al.* A pomegranate-inspired nanoscale design for large-volume-change lithium battery anodes. *Nat. Nanotechnol.* **9,** 187–192 (2014).
17. Zhu, C., Guo, S., Fang, Y. & Dong, S. Reducing sugar: new functional molecules for the green synthesis of graphene nanosheets. *ACS Nano* **4,** 2429–2437 (2010).
18. Akhavan, O., Ghaderi, E., Aghayee, S., Fereydooni, Y. & Talebi, A. The use of a glucose-reduced graphene oxide suspension for photothermal cancer therapy. *J. Mater. Chem.* **22,** 13773–13781 (2012).
19. Soni, S., Brotons, G., Bellour, M., Narayanan, T. & Gibaud, A. Quantitative SAXS analysis of the P123/water/ethanol ternary phase diagram. *J. Phys. Chem. B* **110,** 15157–15165 (2006).
20. Zhou, Y., Bao, Q., Tang, L. A. L., Zhong, Y. & Loh, K. P. Hydrothermal dehydration for the "green" reduction of exfoliated graphene oxide to graphene and demonstration of tunable optical limiting properties. *Chem. Mater.* **21,** 2950–2956 (2009).
21. Ai, W. *et al.* A novel graphene-polysulfide anode material for high-performance lithium-ion batteries. *Sci. Rep.* **3,** 2341 (2013).
22. Ren, L. *et al.* 3D hierarchical porous graphene aerogel with tunable meso-pores on graphene nanosheets for high-performance energy storage. *Sci. Rep.* **5,** 14229 (2015).
23. Ferrari, A. C. & Robertson, J. Interpretation of Raman spectra of disordered and amorphous carbon. *Phys. Rev. B* **61,** 14095–14107 (2000).
24. Dieguez, A., Romano-Rodrıguez, A., Vila, A. & Morante, J. The complete Raman spectrum of nanometric SnO$_2$ particles. *J. Appl. Phys.* **90,** 1550–1557 (2001).
25. Wang, C. *et al.* Ultrathin SnO$_2$ nanosheets: oriented attachment mechanism, nonstoichiometric defects, and enhanced lithium-ion battery performances. *J. Phys. Chem. C* **116,** 4000–4011 (2012).
26. Wang, Y. *et al.* Designed hybrid nanostructure with catalytic effect: beyond the theoretical capacity of SnO$_2$ anode material for lithium ion batteries. *Sci. Rep.* **5,** 9164 (2015).
27. Son, Y. *et al.* Quantum confinement and its related effects on the critical size of GeO$_2$ nanoparticles anodes for lithium batteries. *Nano Lett.* **14,** 1005–1010 (2014).
28. Yang, S., Yue, W., Zhu, J., Ren, Y. & Yang, X. Graphene-based mesoporous SnO$_2$ with enhanced electrochemical performance for lithium-ion batteries. *Adv. Funct. Mater.* **23,** 3570–3576 (2013).
29. Aurbach, D. Review of selected electrode–solution interactions which determine the performance of Li and Li ion batteries. *J. Power Sources* **89,** 206–218 (2000).
30. Hummers Jr, W. S. & Offeman, R. E. Preparation of graphitic oxide. *J. Am. Chem. Soc.* **80,** 1339–1339 (1958).

Acknowledgements

Author Contributions

C.Z. and S.Z. proposed the study and designed the synthesis route. C.Z., K.Z. and Z.H. performed the experiment. H.P. and Y.L. helped to optimize it. C.Z. analyzed experimental data, processed images, drew the schematic of the synthesis route and wrote the article. S.Z., Z.C., D.Z. and D.-W.W. provided revisions to complete the article.

Additional Information

Supplementary information accompanies this paper at http://www.nature.com/srep

Competing financial interests: The authors declare no competing financial interests.

How to cite this article: Zhu, C. *et al.* Confined SnO$_2$ quantum-dot clusters in graphene sheets as high-performance anodes for lithium-ion batteries. *Sci. Rep.* **6,** 25829; doi: 10.1038/srep25829 (2016).